Accepted manuscript on ACS Appl. Mater. Interfaces 2017, 9, 23164−23174.
DOI: 10.1021/acsami.7b04919

Ambipolar MoS_2 transistors by nanoscale tailoring of Schottky barrier using oxygen plasma functionalization

Filippo Giannazzo[1,*], Gabriele Fisichella[1], Giuseppe Greco[1], Salvatore Di Franco[1], Ioannis Deretzis[1], Antonino La Magna[1], Corrado Bongiorno[1], Giuseppe Nicotra[1], Corrado Spinella[1], Michelangelo Scopelliti[2,3,4], Bruno Pignataro[2,3], Simonpietro Agnello[2,3], Fabrizio Roccaforte[1]

[1] *CNR-IMM, Strada VIII, 5, 95121 Catania, Italy.*

[2] *Dipartimento di Fisica e Chimica (DiFC) - Università degli Studi di Palermo - Viale delle Scienze, Ed. 17 - 90128 Palermo, Italy*

[3] *Aten Center, Università di Palermo, Ed. 18 V.le delle Scienze, Parco d'Orleans II 90128 Palermo, Italy*

[4] *Consorzio Interuniversitario di Ricerca in Chimica dei Metalli nei Sistemi Biologici (C.I.R.C.M.S.B.) - 1, Piazza Umberto I - 70121 Bari, Italy*

Abstract

One of the main challenges to exploit molybdenum disulfide (MoS_2) potentialities for the next generation complementary-metal-oxide-semiconductor (CMOS) technology is the realization of p-type or ambipolar field effect transistors (FETs). Hole transport in MoS_2 FETs is typically hampered by the high Schottky barrier height (SBH) for holes at source/drain contacts, due to the Fermi level pinning close to the conduction band. In this work, we show that the SBH of multilayer MoS_2 surface can be tailored at nanoscale using soft O_2 plasma treatments. The morphological, chemical, and electrical modifications of MoS_2 surface under different plasma conditions were investigated by several microscopic and spectroscopic characterization techniques, including X-ray Photoelectron Spectroscopy (XPS), Atomic Force Microscopy (AFM), Conductive AFM (CAFM), aberration-corrected Scanning Transmission Electron Microscopy (STEM) and Electron Energy Loss Spectroscopy (EELS). Nanoscale current-voltage mapping by CAFM showed that the SBH maps can be conveniently tuned starting from a narrow SBH distribution (from 0.2 to 0.3 eV) in the case of pristine MoS_2 to a broader distribution (from 0.2 to 0.8 eV) after 600 s O_2 plasma treatment, which allows both electron and hole injection. This lateral

inhomogeneity in the electrical properties was associated to variations of the incorporated oxygen concentration in the MoS_2 multilayer surface, as shown by STEM/EELS analyses and confirmed by ab-initio density functional theory (DFT) calculations. Back-gated multilayer MoS_2 FETs, fabricated by self-aligned deposition of source/drain contacts in the O_2 plasma functionalized areas, exhibit ambipolar current transport with on/off current ratio $I_{on}/I_{off} \approx 10^3$ and field effect mobilities of 11.5 $cm^2V^{-1}s^{-1}$ and 7.2 $cm^2V^{-1}s^{-1}$ for electrons and holes, respectively. The electrical behavior of these novel ambipolar devices is discussed in terms of the peculiar current injection mechanisms in the O_2 plasma functionalized MoS_2 surface.

Keywords: MoS_2, ambipolar transistors, Schottky barrier, conductive atomic force microscopy, atomic resolution STEM, DFT calculations

e-mail: filippo.giannazzo@imm.cnr.it

Introduction

Semiconducting two-dimensional transition metal dichalchogenides (TMDs), including MoS_2, WS_2, $MoSe_2$, WSe_2, are currently subject of high scientific and technological interest, as they represent a viable solution for post-Si complementary metal oxide semiconductor (CMOS) technology. To date MoS_2 has been the most widely investigated member of the TMDs' family, due to its relatively low cost, abundance in nature as bulk mineral (Molybdenite), and chemical stability after exfoliation. Multilayers MoS_2 exhibit an indirect bandgap of ~1.2 eV, whereas ~1.8 eV direct bandgap is observed for monolayer samples. Field effect transistors (FETs) with very interesting performances in terms of on/off current ratio (10^6-10^8) and low subthreshold swing (SS~70 meV/decade) have been already demonstrated both with single layer [1] and with multilayers of MoS_2 [2]. Furthermore, ultra-scaled MoS_2 FETs with 1 nm gate length [3] or with sub-10 nm channel lengths [4] have been recently reported, further supporting the expectations for MoS_2 transistors beyond the technology road map [5].

In spite of these great promises, several issues need to be addressed to develop a MoS_2-based CMOS technology. MoS_2 thin films, produced either by exfoliation from the bulk crystal or by chemical vapour deposition (CVD) methods, are typically unintentionally n-type doped. Furthermore, most of the elementary metals exhibit a Fermi level pinning close to MoS_2 conduction band, resulting in relatively low values of the Schottky barrier height (SBH) for electrons injection in MoS_2, typically ranging from

20-60 meV for low workfunction metals (Sc, Ti,...) to 150 - 250 meV for high workfunction ones (Ni, Pt,..) [6]. The origin of this Fermi level pinning is still matter of debate, although some nanoscale electrical investigations (based on scanning tunnelling microscopy or conductive atomic force microscopy) highlighted the possible role of the defects present at the MoS_2 surface [7,8]. As a matter of fact, the low SBH for electrons translates into a high SBH for holes. Hence, n-type FETs with an electron accumulation channel can be easily obtained with unintentionally n-type doped MoS_2, and low resistance contacts have been achieved either using low workfunction metals [6] or by selective area modification of 2H-MoS_2 to the 1T-MoS_2 metallic phase in the source/drain contact regions [9,10]. On the other hand, the fabrication of MoS_2 FETs with the complementary p-type behaviour is challenging, due to the difficulty to inject holes in the inversion channel [11,12].

Selective-area p-type doping of MoS_2 under the source/drain electrodes and/or the use of unconventional contacts forming a low Schottky barrier for holes injection are required to develop a CMOS technology on MoS_2. To date several approaches have been explored in the literature to reach this goal. As an example, substoichiometric MoO_x (with $2<x<3$) contacts were demonstrated to be effective for hole injection into pristine MoS_2, due to the high MoO_x work-function. Both p-type transistors and p-n diodes have been fabricated by selective-area deposition of MoO_x layers [13]. However, an accurate control of the deposition conditions (MoO_x purity and stoichiometry) and of the interface chemistry are required for an efficient hole injection from MoO_x ohmic contacts into MoS_2 and other TMDs [14]. Several doping strategies for MoS_2 have been considered in the literature [15]. As an example, incorporation of substitutional Nb atoms (replacing Mo cations) during CVD growth of MoS_2 proved to be an effective way to achieve stable and high concentration p-type doping of this material [16], and p-type transistors with a hole accumulation channel have been recently demonstrated with Nb-doped MoS_2 multilayers [17]. However, substitutional doping during the CVD growth lacks of area selectivity. Recently, low energy phosphorus plasma immersion ion implantation was used for selective area p-type doping of multilayer MoS_2, with the doping effect explained by charge transfer originating from substitutional as well as physisorbed phosphorus in top few layers of MoS_2 [18]. p-type chemical doping of MoS_2 by gold chloride ($AuCl_3$) has been also recently demonstrated, and multilayer MoS_2 back-gated FETs with hole conduction have been fabricated by spin coating of an $AuCl_3$ solution on the channel region [19]. This doping method can be, in principle, selectively applied to individual transistors on a wafer, and a proof of concept CMOS inverter was obtained by coupling a pristine MoS_2 n-FET and an $AuCl_3$ chemically doped p-FET [19]. However, in the perspective of running MoS_2 devices fabrication in a Si-CMOS

production line, the adoption of such a solution would be hampered by the need to avoid Au contaminations issues.

In the last few years, plasma treatments with different species (including O_2, CHF_3, CF_4, SF_6) have been also investigated by several research groups to achieve controlled modifications of MoS_2 electrical/optical properties [20,21,22,23,24,25], as these methods are fully compatible with current semiconductor technology. However, the detailed structural/chemical mechanisms of MoS_2 electrical modification during the exposure to these different plasma species are still largely unclear. In particular, the role played by MoS_2 chemical modifications and by defects introduced by energetic ions needs a deeper investigation. Among the various plasma treatments of MoS_2 considered so far, O_2 plasma received the largest attention. According to recent literature reports, very different results can be achieved depending on the plasma conditions (*i.e.*, high power plasma or soft plasma treatments), and on the thickness of the MoS_2 sample (*i.e.*, single- or multi-layer).

In the case of a single layer MoS_2, it has been reported that the main effect of O_2 plasma treatment is an increase of the sheet resistance by several orders of magnitude with the increase of the plasma exposure time, with a resulting transition from the semiconducting to the insulating transport regime [20]. These changes in the electrical properties of the single layer MoS_2 sheet were ascribed to the formation of insulating MoO_3-rich disordered nanometric domains, surrounded by MoS_2 regions with significant lattice distortion [20]. A similar transition from semiconducting to insulating behaviour has been reported also in the case of few layers MoS_2 films (from 1 up to 8 layers) [21]. These results were explained assuming that the energetic oxygen from the plasma not only interacts with the surface atoms but also propagates deeply inside the layers to create MoO_3 defects in the few layers MoS_2. The transport properties of such defected systems were described as an effective medium semiconductor with a bandgap higher than MoS_2. Oxygen plasma exposure was also used to strongly modify the optical properties of single-layer MoS_2, giving rise either to a strong enhancement [22] or to the quenching [23] of the photoluminescence. These very different results were ascribed (according to DFT calculations [22]) to different oxygen bonding configurations, resulting from different plasma conditions. In the case of multilayer MoS_2 samples subjected to energetic O_2 plasma treatments, a p-type doping of the exposed areas has been demonstrated by the fabrication of MoS_2 lateral p-n diodes with good rectifying behaviour [24]. However, the detailed mechanisms of the doping effect are still not clear. Furthermore, when performing energetic plasma treatments, the exposed multilayer MoS_2 areas can undergo a significant etching [24], this being a drawback for the realization of MoS_2 FETs with a thin channel region. Hence, soft plasma treatments are strongly

required to achieve a controlled modification of MoS_2 electrical properties, minimizing the etching effects. As an example, a recent study of multilayer MoS_2 treatment with a remote O_2 plasma demonstrated the possibility of selective chemical modification of the topmost MoS_2 layer, without altering the composition of the underlying film [26]. XPS analyses showed that the surface oxidation process during these soft plasma treatments proceeds through the formation of sub-stoichiometric MoO_x up to the uniform coverage by a monolayer of amorphous MoO_3 after long exposure to the plasma. Interestingly, a gradual shift of the Fermi level toward the valence band was observed with increasing the exposure time, indicating a p-type doping of underlying MoS_2 [26].

In this paper, we demonstrate the ambipolar behaviour in multilayer MoS_2 transistors by nanoscale tailoring of the Schottky barrier with MoS_2 surface in the source/drain areas using soft O_2 plasma treatments. A detailed study, based on the combination of several microscopic and spectroscopic characterization techniques (including XPS, AFM, CAFM and aberration-corrected STEM/EELS), elucidated the morphological, chemical, and electrical modification of the MoS_2 surface under different plasma conditions. In particular, nanoscale electrical analyses by CAFM showed how the SBH and doping can be tailored by increasing the plasma exposure time. Starting from a narrow distribution of low SBHs for electrons in the case of pristine MoS_2, the SBH map was modified after 600 s O_2 plasma treatment into a broader distribution formed by nanometric patches with low SBH for holes (due to local p-type doping) inside a background with low SBH for electrons. These lateral inhomogeneities of the electrical properties in O_2 plasma treated samples are associated to lateral variations of the incorporated oxygen concentration in the MoS_2 multilayer surface, as indicated by STEM/EELS analyses and ab-initio DFT calculations. Back-gated multilayer MoS_2 field effect transistors were fabricated by self-aligned deposition of Ni/Au source/drain contacts in the O_2 plasma functionalized areas.
Differently than pristine MoS_2 transistors (with n-type behaviour), these devices exhibit both electron transport (for $V_G>0$) and hole transport (for $V_G<0$), with on/off current ratio $I_{on}/I_{off} \approx 10^3$ and field effect mobilities of 11.5 $cm^2V^{-1}s^{-1}$ and 7.2 $cm^2V^{-1}s^{-1}$ for electrons and holes, respectively.

Results and Discussion

Multilayer MoS_2 flakes exfoliated from bulk molybdenite were subjected to surface functionalization by a soft O_2 plasma, which was generated by a source located far from the sample. No bias was applied to the sample during the treatment to avoid physical etching. The effect of different plasma exposure times

on the surface chemistry, morphology and nanoscale electrical properties of MoS_2 were preliminarily evaluated by X-ray Photoelectron Spectroscopy (XPS), atomic force microscopy (AFM) and conductive atomic force microscopy (CAFM). Fig.1 shows the surface morphology of pristine (*i.e.*, as-exfoliated) MoS_2 (a), and of MoS_2 samples subjected to O_2 plasma for 300 s (b), 600 s (c) and 1200 s (d). The root mean square (RMS) roughness values, calculated from the four topography maps, are also reported in the figures. Only a limited increase in the roughness (from 0.11 to 0.18 nm) is observed upon increasing the plasma exposure time from t=0 s to 600 s, whereas a more significant roughening (RMS=0.26 nm) is found after 1200 s O_2 plasma treatment. Representative height line-scans extracted from the AFM images are shown in Fig.1 (e)-(h). It can be observed that for plasma exposure times up to 600 s the peak-to-valley height excursion is less than the thickness of a MoS_2 monolayer (≈0.7 nm).

In order to investigate the changes in the surface chemistry occurring as a consequence of the different plasma treatments, XPS spectra of Mo *3d*, S *2s* and S *2p* regions have been collected from each sample. Results are reported in Fig.2, whereas spectral features are summarized in Table S1 of the Supporting Information. The Binding Energy (BE) values are reported with respect to C *1s* C–C/C–H peak (284.8 eV), taken as a reference (see Fig.S1 in the Supporting Information). The Mo *3d* and S *2s* spectra of the pristine sample demonstrate a nearly clean MoS_2 surface and the S *2p* spectral range shows that S is bound only to Mo. After the 300 s O_2 plasma treatment, oxidation of the MoS_2 surface is observed. In particular, the presence of two different Mo-oxide species, *i.e.*, Mo^{6+} (~ 233 eV) and an intermediate oxidation state $Mo^{(6-x)+}$ was deduced by deconvolution of the Mo *3d* spectra, along with the appearance of the S–O bond from S *2p* spectra. On the other hand, Mo^{4+} (228.7-229.5 eV) [27,28] and Mo^{5+} (231.0-231.5 eV) [28,29,30] oxidation states are not observed. Interestingly, both S *2p* and Mo *3d* regions (including S *2s* peak) are shifted by –0.4 eV with respect to the as-exfoliated sample, but the relative peak positions are maintained. A larger negative shift (0.7 eV) of the peaks is observed after 600 s O_2 plasma treatment. Finally, no significant differences are observed between the spectra acquired after 600 and 1200 s plasma processes. Analogous rigid shifts have been previously reported [26] and ascribed to a Fermi level shift towards the valence band (*i.e.*, to a p-type doping effect of MoS_2) due to surface oxidation. Micro-Raman measurements on pristine multilayer MoS_2 and after O_2 plasma treatment (1200 s) are also reported in the Supporting Information (Fig.S2). The E^1_{2g} and A_{1g} bands of MoS_2 are almost overlapped for the two samples. Moreover, the bands at about 225 cm^{-1} or at 820 cm^{-1} attributable to MoS_2 bulk oxidation or formation of MoO_3 [23,31,32] were not detected. These findings are consistent with the fact that only the

surface of multilayer MoS_2 is chemically modified by the plasma process, whereas the underneath layers (which give the main contribution to the Raman signal) are not affected by the oxidative processes.

In order to understand the effect of these surface chemical modifications on the electrical properties of MoS_2, we first performed nanoscale current mapping by conductive atomic force microscopy (CAFM). Measurements were performed on multilayer MoS_2 flakes (with typical thickness from 30 to 60 nm, as evaluated by AFM) exfoliated on SiO_2 (380 nm)/Si substrates. Ad-hoc test patterns were lithographically defined on the flakes, consisting of open MoS_2 circular regions surrounded by a large metal (Ni/Au) contact, as illustrated in the inset of Fig.3(a). Four different samples have been prepared with these test structures, and three of them have been subjected to the O_2 plasma treatments for 300, 600 and 1200 s, respectively. A sharp metal (Pt)-coated AFM tip (with 10 nm contact radius) was scanned on MoS_2 on a square array of positions. For each tip position, a bias ramp is applied to the macroscopic metal contact and the current flowing through the MoS_2 film from the nanometric tip to the macroscopic contact is recorded by a current sensor connected to the tip. In this measurement configuration, the main resistance contributions to the measured current are the tip/MoS_2 contact resistance and the spreading resistance in the nanometric MoS_2 region around the tip [8]. This ensures the possibility of locally probing both current injection into MoS_2 (*i.e.*, the SBH) and resistivity with nanoscale lateral resolution. Fig.3 reports representative current-voltage characteristics collected on arrays of 5×5 tip positions with 50 nm spacing for the pristine MoS_2 sample (a) and for the samples subjected to O_2 plasma for 300 s (e) and 600 s (i). Measurements on the sample subjected to 1200 s plasma treatment are shown in Fig.S3 of the Supporting Information. For the sake of simplicity, the applied bias is referred to the tip (V_{tip}). Using this convention, the tip in contact with n-type doped MoS_2 is expected to form a forward biased nano-Schottky junction for $V_{tip}>0$ and a reverse biased junction for $V_{tip}<0$. On the other hand, in the presence of p-type doped MoS_2 regions, the nano-Schottky will be forward biased for $V_{tip}<0$ and reverse biased for $V_{tip}>0$.

The local I-V_{tip} characteristics collected on the pristine sample (Fig.3(a)) exhibit the typical behavior observed for low Schottky barrier height contacts on n-type MoS_2, with a current onset at low forward bias ($V_{tip}>0$) and a high leakage current under reverse bias ($V_{tip}<0$) [8]. In the upper left inset of Fig.3(a), a representative forward bias characteristic is also reported both on semilog scale (left axis) and linear scale (right axis). A linear increase of the current with the bias over more than two decades, followed by a saturation due to series resistance R, can be observed in the semilog plot. The SBH value ($\Phi_{B,n}$=0.31 eV) and the ideality index (n=1.05) were extracted by the fitting of the linear region of this curve with the thermionic emission equation

$$I = A_{tip} A^* T^2 \exp\left(-\frac{\Phi_{B,n}}{kT}\right)\exp\left(\frac{qV_{tip}}{nkT}\right), \quad (1)$$

being $A_{tip}=\pi r_{tip}^2$ the tip contact area, T=300 K, k the Boltzmann constant, q the electron charge and A^* the Richardson constant of multilayer MoS_2 [8]. The series resistance contribution (R≈0.9 MΩ) was estimated by linear fitting of the linear scale I-V_{tip} characteristic (right axis) for V_{tip} above the onset voltage. This series resistance contribution is mainly associated to the local resistivity of MoS_2 in the nanometric size volume under the tip. Fig.3(b) and (c) report two-dimensional (2D) maps of the SBH $\Phi_{B,n}$ and of series resistance R evaluated by fitting a square array of 10×10 I-V_{tip} curves acquired over 0.5×0.5 μm scan area. Furthermore, the histograms of the R and Φ_B values extracted from each I-V_{tip} curve is reported in Fig.3(d). For pristine MoS_2 $\Phi_{B,n}$ values are found to be in the range from 0.23 to 0.35 eV and the R values from 0.4 to 1.1 MΩ. A schematic band-diagram for the Schottky contact on pristine MoS_2 is also reported in the inset of Fig.3(d), higher panel.

After 300 s plasma treatment (Fig.3(e)), the I-V_{tip} characteristics still maintain the typical shape for Schottky contacts on n-type MoS_2, but a larger spread between the locally measured curves can be observed, both in the forward (V_{tip}>0 V) and reverse bias (V_{tip}<0 V) polarization. This is the result of a broader distribution of the Schottky barrier height ($\Phi_{B,n}$ ranging from 0.21 to 0.58 eV) and of the series resistance values (R ranging from 0.6 to 1.7 MΩ) after the soft plasma treatment, as shown by the $\Phi_{B,n}$ and R maps (Fig.3(f) and (g)), as well as by the histograms of the $\Phi_{B,n}$ and R values in Fig.3(h). As a matter of fact, since the metal contact used for the measurements is unchanged with respect to the case of pristine MoS_2, the higher values of the local SBH can be only ascribed to a shift of the Fermi level from the conduction towards the valence band of MoS_2. Noteworthy the results of this nanoscale electrical characterization are consistent with the average results deduced from macroscopic XPS analyses. A schematic representation of the band-diagram for the Schottky contact on O_2 functionalized MoS_2 is also reported in the inset of Fig.3(h), higher panel.

The 600 s long O_2 plasma treatment introduces further modifications in the local I-V_{tip} characteristics. As shown in Fig.3(i), in addition to n-type Schottky diode curves, some curves (drawn in red) with the typical behavior for Schottky contacts on a p-type semiconductor can be observed (*i.e.*, the onset of a negative current at V_{tip}<0 and negligible current for V_{tip}>0). The Schottky barrier height for holes $\Phi_{B,p}$ can be extracted by fitting |I|-V_{tip} on semilog-scale (for V_{tip}<0) with the thermionic emission law, as illustrated in the image in the lower-right inset of Fig.3(i). For this representative |I|-V curve, a SBH for

holes $\Phi_{B,p}$=0.49 eV was obtained, which corresponds to a SBH for electrons of $\Phi_{B,n}$≈0.71 eV, according to the relation:

$$\Phi_{B,n}=E_g-\Phi_{B,p} \quad (2)$$

where E_g is the bandgap of multilayer MoS_2. Clearly, values of $\Phi_{B,n}>E_g/2$ correspond to a p-type doped MoS_2, as schematically illustrated in the inset of Fig.3(n), higher panel. The map of the $\Phi_{B,n}$ values reported in Fig.3(l), along with the histogram in Fig.3(n), higher panel, indicate the occurrence of p-type doping on ~16% of the MoS_2 area exposed to O_2 plasma. Only a limited increase of R is observed after the 600 s plasma treatment with respect to the 300 s long process, as deduced from the 2D map of the R values in Fig.3(m) and from the histogram in Fig3(n), lower panel.

On the other hand, the sample subjected to 1200 s long O_2 plasma exposure showed a very large spread of local I-V_{tip} curves (both with n- and p-type Schottky behavior), accompanied by a strong increase of the series resistance (up to 7 MΩ), as shown in Fig.S3 of the Supporting Information. The significant increase of the surface roughness (shown by AFM in Fig.1(d)) and this strong increase of the series resistance indicate a degradation of the surface structural properties. Hence, the 600 s long O_2 plasma treatment was chosen as the optimal condition to achieve both electrons and holes current injection under the contacts.

It should be noted that the correlation of low $\Phi_{B,p}$ values with a local p-type doping of MoS_2 is peculiar for MoS_2 subjected to the O_2 plasma functionalization process. Generally speaking, doping of a semiconductor and change in its SBH are two different phenomena, that are not necessarily correlated, and it can be possible to have a combination of p-type doped material and $\Phi_{B,n}<\Phi_{B,p}$ or vice-versa.

Fig.4(a) and (b) shows two atomic resolution STEM analyses at different magnifications performed close to the edge of a multilayer MoS_2 flake subjected to this optimal O_2 plasma condition. It is worth noting that oxygen atoms are incorporated only in the topmost layer of this multilayer. Due to this reason and to the low atomic number of oxygen, the contrast in atomic resolution STEM images is associated to the stacking of columns of Mo and S atoms in the multilayer, whereas substitutional O atoms in the surface cannot be visible. On the other hand, these measurements confirm how the structural properties of the MoS_2 lattice are preserved by the soft plasma process. In order to get local chemical analyses with sub-nanometric resolution, EELS measurements were also carried out on the MoS_2 flakes using a 60 keV primary electron beam. Fig.4(c) shows representative EELS spectra collected on pristine MoS_2 samples (reference) and on MoS_2 flakes subjected to 600 s O_2 plasma treatment (performed directly on the flakes

attached to the TEM grid). Here, subtraction of the background signal and plural scattering deconvolution have been performed by applying the power-law background fitting and Fourier-ratio method, respectively. As a reference, a DFT simulated EELS spectrum for pristine MoS_2 has been also included (details on the EELS spectra simulations are reported in the Materials and Methods section). In the energy region between 385 and 565 eV, three characteristics ionization edges for Mo (*i.e.*, $M_{1,2}$ and M_3) can be identified both on the pristine and on the O_2 plasma treated sample. Noteworthy, the positions of the most prominent Mo-$M_{2,3}$ ionization edges in the experimental EELS spectra of pristine MoS_2 are coincident with those on the simulated one, indicating a right calibration of the energy scale. An energy shift of the $M_{2,3}$ peaks toward higher energies, accompanied by the appearance of the oxygen-related O-K edge, can be observed in the sample subjected to 600 s O_2 plasma treatment, indicating the formation of oxidized Mo on the flake surface [33]. These characteristic spectra can be found all over on the sample surface but with a variable intensity of the O-K peak, indicating a laterally inhomogeneous incorporation of oxygen on the MoS_2 surface. Fig.4(d) shows a Z-contrast image collected at low magnification on a multilayer MoS_2 flake. The dark grey patches in this image are due to sub-monolayer etched areas on MoS_2 surface produced by the soft O_2 plasma, which are also responsible of the roughness in the AFM image of Fig.1(c). The size and the density of these patches are similar to those of the high SBH (*i.e.* p-type doped) areas in the electrical map of Fig.3(l). In order to obtain maps of the oxygen distribution with sub-nanometric resolution, spectrum images (dataset containing both Z contrast and EELS data) have been also acquired on several positions of the flakes. The oxygen map was extracted from these data by integration of the EELS signal around the O-K edge. As an example, Fig.4(e) shows a representative image collected at the edge of a patch area, where the oxygen map (red contrast) is overlapped to the Z-contrast map (light blue), related to the surface morphology. Intensity line-scans of oxygen concentration and Z-contrast are also reported in Fig.4(f), showing that the oxygen incorporation can be partially related to the morphology. By statistics on several spectrum images, oxygen accumulation at the edges of the patches was detected.

High resolution chemical mapping by STEM/EELS indicate a laterally inhomogeneous oxygen incorporation in the MoS_2 surface. To understand if such surface compositional inhomogeneity can be the origin of the lateral inhomogeneous distribution in the SBH observed by CAFM nanoscale electrical analyses, ab-initio DFT calculations of the energy bandstructure were performed (see the details in the Materials and Methods section). In order to reproduce a system similar to the experimental one, a few layers MoS_2 system was considered in the simulations and oxygen atoms were assumed to be bound only to the topmost layer. The effect of different oxygen bonding configurations on the electronic

bandstructure of the whole system was considered. First, the effect of oxygen adatoms lying on top of S atoms was simulated and it could not account for the experimentally observed local p-type doping of MoS_2, as discussed in the Supporting Information (Fig. S4). On the other hand, replacement of S with O atoms in substitutional configurations inside the topmost layer was found to justify a p-type doping effect of underlying MoS_2 layers, as illustrated in the following. Fig.5 shows the structural configuration and electronic structure calculations for a trilayer of MoS_2 with four different atomic percentage of substitutional oxygen included in the topmost layer: 0%, *i.e.* pristine MoS_2 (a), 11.1% (b), 22.2% (c), 33.3% (d). Here, substitution of oxygen to sulfur atoms produces only local lattice distortions in the topmost layer, without changing the overall lattice structure. Hence, this topmost layer can be described as a MoO_xS_{2-x} alloy with variable oxygen fraction x from 0 to 0.33. In the case of 0% substitutional oxygen, an indirect bandgap of 1.1 eV and a charge neutral system (with the Fermi level lying at midgap) is predicted by DFT calculations in Fig.5(a), right panel. For substitutional oxygen percentages from 11.1 to 33.3%, the electronic bandstructure of the topmost MoO_xS_{2-x} layer and of the underlying MoS_2 bilayer are depicted in red and green, respectively, as illustrated in the right panels of Fig.5(b), (c) and (d). It should be noted that, with increasing the oxygen content, the bandgap of the MoO_xS_{2-x} layer decreases (down to ~0.2 eV for 33.3% oxygen), its valence band stays aligned with that of underlying MoS_2, and the Fermi level of the whole systems stays pinned at MoO_xS_{2-x} midgap. This trend is illustrated in Fig.5(e). As a result, a gradual shift of the Fermi level towards the valence band, *i.e.*, an increasing p-type doping of the system, is predicted by increasing the substitutional oxygen incorporation in the topmost layer. The results of these DFT calculations allows to account for a laterally inhomogeneous p-type doping due to lateral variations of incorporated oxygen in the MoS_2 surface, as indicated by nanoscale resolutions chemical maps obtained by EELS. The scenario considered in the simulations, *i.e.*, the formation of a MoO_xS_{2-x} alloy on the surface of multilayer MoS_2 subjected to a soft O_2 plasma is the most realistic one, considering that the crystalline structure of MoS_2 appears to be preserved, according to atomic resolution STEM analyses in Fig.4(a) and (b). Another possible scenario, *i.e.*, the transformation of the MoS_2 topmost layer into a MoO_3 (with a different lattice structure than MoS_2) has been also considered, by performing the DFT electronic structure calculation of the MoO_3/MoS_2 heterojunction (see Supporting Information, Fig.S5 and S6). Also in this case a p-type doping effect of MoS_2 is predicted by simulations, but the origin is very different and resides in the very high work-function of the MoO_3 insulator. Although MoS_2 p-type doping could be accounted also by this scenario, the presence of a thin insulator on MoS_2 would introduce a high tunnel resistance contribution for current

injection in MoS_2. This is not consistent with the CAFM results obtained for samples subjected to the optimized soft plasma treatment.

To understand the implications on devices electrical characteristics of the nanoscale modification of MoS_2 surface properties induced by the O_2 plasma, we fabricated back-gated field effect transistors with source and drain contacts deposited on pristine MoS_2 (see schematic illustration in Fig.6(a)) or on areas selectively exposed to O_2 plasma functionalization (see schematic in Fig.6(b)). The 600 s long plasma treatment was adopted, as it results in the occurrence of both n and p type doped areas without a strong degradation of MoS_2 resistance. Fig.6(c) shows the output characteristics I_D-V_{DS} for different gate bias values (V_G from -60 to 20 V) measured on a FET with channel length L=10 μm fabricated with a ~40 nm thick pristine MoS_2 flake (see optical microscopy in the inset). In the plot, the current value is normalized to the channel width W, to have a direct comparison between devices with different W. All the I_D-V_{DS} curves exhibit a linear behavior for small V_{DS} values, with the slope monotonically increasing with V_G. The saturation of I_D at higher V_{DS} is observed only for low V_G values (as indicated in Fig.6(c)), for which the pinch off the channel occurs. The transfer characteristiscs I_D-V_G for different drain bias values (V_{DS}=1, 2 and 5 V) are reported on a semilog-scale in Fig.6(d). The n-type transistor behavior typically reported for MoS_2 FETs can be observed, with a monotonic increase of the I_D over more than 5 decades in the considered gate bias range. The exponential increase of I_D with V_G at high negative bias values (i.e. $V_G<V_{FB}$, with V_{FB} the flatband voltage) is due to thermionic emission of electrons above the Schottky barrier at Ni/MoS_2 interface, whereas thermionic field emission and tunneling through the barrier occurs at for $V_G>V_{FB}$. Hence, the effective SBH can be determined from temperature dependent measurements of the I_D-V_G characteristics, separating the contribution of thermionic emission and tunneling currents [6]. We recently performed this kind of analysis on Ni/Au contacts deposited on pristine MoS_2, and the obtained effective SBH value was ~0.18 eV [34], slightly lower than the values extracted by fitting of the local I-V curves measured by CAFM with the thermionic emission law.

A linear scale plot of the transfer characteristic (measured with V_{DS}=5 V) is also reported in Fig.6(e). By fitting of the linear region in the I_D-V_G curve, the threshold voltage for electron accumulation in the channel ($V_{th,n}$=-35 V) was obtained as the intercept with the horizontal axis, and the field effect mobility ($\mu_e \approx 30\ cm^2V^{-1}s^{-1}$) was evaluated as:

$$\mu_e = \frac{g_m}{W}\frac{L}{C_{ox}V_{DS}} \qquad (3)$$

being g_m/W the slope of the I_D-V_G curve and C_{ox} the SiO_2 gate oxide capacitance.

Fig.6(f) and (g) show the output characteristics of a MoS_2 transistor with the same channel length (L=10 μm) and thickness (~40 nm) of the pristine one, but with the source and drain contacts deposited on plasma O_2 functionalized regions. While the set of I_D-V_{DS} curves measured for $V_G>0$ (see Fig.6(f)) exhibit an increase of the current with increasing V_G (as typically observed for n-type transistors), a decrease of I_D with increasing V_G is observed for the set of I_D-V_{DS} characteristics measured for $V_G<0$ (see Fig.6(g)), indicating a p-type behavior. Differently than in the case of the pristine MoS_2 FET, the n-type output characteristics (Fig.6(f)) exhibit an onset voltage at $V_{DS}\approx 2V$ and negligible current below this voltage. The suppressed electron current for low V_{DS} can be explained by the space charge region around the nanoscale p-type doped patches below source and drain, resulting in a pinch-off of the conduction paths for electrons from the contacts to the n-type channel. The extension of this space charge volume is progressively reduced with increasing V_{DS} up to the current onset at V_{DS}=2V. The p-type I_D-V_{DS} characteristics measured for $V_G<0$ (Fig.6(g)) exhibit a much lower onset voltage, and a linear increase of I_D vs V_{DS} up to $V_{DS}\approx 0.7V$ (where a kink in the I_D-V_{DS} curves is observed), followed by a nearly saturating behavior for $V_{DS}>0.7V$. Accurate device simulations will be carried out to quantitatively describe the output characteristics behavior both for $V_G>0$ and for $V_G<0$. Such a behavior is reflected in the device transfer characteristics I_D-V_G, reported in Fig.6(h) on semilog scale for V_{DS}=1, 2 and 5 V and in Fig.6(i) on a linear scale for V_{DS}=5V. In particular, for V_{DS}=1V and 2V, the transfer characteristics exhibit a pronounced p-type behavior, with the hole current branch (for $V_G<0$) significantly higher than the electron current branch (for $V_G>0$), whereas for V_{DS}=5V an ambipolar behavior is observed, with I_{on}/I_{off} current ratio $\approx 10^3$ for both the electrons and holes branches. The lower I_{on}/I_{off} current ratio with respect to pristine MoS_2 FETs is mostly due the higher off-state current and, in part, to a reduced current drive in the on-state. Clearly, the off-state current level depends on the peculiar current transport mechanisms in the subthreshold regime, and specifically on the current injection through the nanoscale engineered Schottky barrier by O_2 plasma treatments. An accurate modelling of the electrical characteristics by device simulations will be necessary to quantitatively describe these effects. The linear scale I_D-V_G characteristic in Fig.6(i) exhibits two threshold voltages, one for electrons accumulation ($V_{th,n}\approx 8V$) and the other for the holes inversion channel formation ($V_{th,p}\approx -39$ V). Furthermore, from the slope of the I_D-V_G characteristics in the two branches, the field effect mobilities for electrons (μ_e=11.5 $cm^2V^{-1}s^{-1}$) and holes (μ_h=7.2 $cm^2V^{-1}s^{-1}$) have been evaluated.

Based on the above results, the key to achieve this ambipolar behavior in O_2 functionalized FETs is represented by the coexistence of n-type doped regions (with low SBH for electrons) and p-type doped regions (with low SBH for holes) within the same source and drain contact areas. In particular, for a positively biased drain contact ($V_{DS}>0$), the injection of electrons from the source to the accumulation channel (for $V_G>0$) occurs through regions with lower SBH for electrons, whereas the injection of holes from the drain to the inversion channel (for $V_G<0$) is allowed by the regions with low SBH for holes. The possibility to have both n- and p- type current transport in a single device structure can be interesting for some digital electronics applications. On the other hand, as the effective area available for electrons (holes) injection is only a fraction of the contact area, this results in reduced current drive (by almost a factor of 10) with respect to pristine MoS_2 devices with the same geometry. The adopted self-aligned fabrication process is fully compatible with CMOS technology and does not suffer of the resolution constrains typically imposed by the overlay of two different lithographic steps imply, allowing (in principle) the scaling of the device to very short channel length. However, lateral permeation of O_2 plasma inter the gap between resist and MoS_2 (starting from the edges of resist covered areas) cannot be excluded, and this could ultimately limit the minimum channel length that can be reached by this self-aligned process.

Conclusion

We demonstrated that the nanoscale Schottky barrier distribution at the surface of multilayer MoS_2 can be tailored by O_2 plasma functionalization, starting from a narrow SBH distribution (0.2 - 0.3 eV) in the case of pristine MoS_2 to a broader distribution (from 0.2 to 0.8 eV) after 600 s plasma treatment. The lateral inhomogeneity in the electrical properties was associated to lateral variations of the incorporated oxygen concentration in the topmost MoS_2 layer. Back-gated multilayer MoS_2 field effect transistors, fabricated by self-aligned deposition of the source/drain contacts in the O_2 plasma functionalized areas, exhibit ambipolar current transport with on/off current ratio $I_{on}/I_{off} \approx 10^3$ and field effect mobilities of 11.5 $cm^2V^{-1}s^{-1}$ and 7.2 $cm^2V^{-1}s^{-1}$ for electrons and holes, respectively. The electrical behavior of these novel ambipolar devices has been discussed in terms of the peculiar current injection mechanisms in the O_2 plasma functionalized MoS_2 surface.

This work sheds light on the possibility of fine tuning metal/MoS_2 electronic properties through a surface pre-functionalization process, which can find many applications for next generation electronic/optoelectronic devices based on this material. Furthermore, the adopted fabrication approach

for the proof-of-concept ambipolar FET is scalable and fully compatible with CMOS technology, making it suitable for ultra-scaled MoS_2 transistors fabrication.

Supporting Information

XPS analyses; Micro-Raman characterization of pristine and O2 plasma treated MoS2 for 1200s; Conductive Atomic Force Microscopy characterization of O2 plasma treated MoS2 for 1200s; DFT calculations.

Acknowledgements

We acknowledge A. Piazza and E. Schilirò (CNR-IMM) for their collaboration with samples preparation. The European Fund Operational Programme for Regional Development of Sicily (PO FESR 2007-2013) is acknowledged for funding by the project MEDETNA. This work has been supported, in part, by the project GraNitE "Graphene heterostructures with Nitrides for high frequency Electronics" (Grant No. 0001411), in the framework of the EU program "FET Flagship ERA-NET" (FLAG-ERA).

Materials and Methods

Samples preparation. MoS_2 samples used in this study were obtained by exfoliation from bulk molybdenite (purchased from SPI). Samples for XPS analyses were obtained exfoliating large area and thick MoS_2 flakes on a metallic substrate (used to avoid charging during measurements). MoS_2 flakes used for the fabrication of back-gated field effect transistors and for nanoscale electrical measurement using CAFM were exfoliated by using a thermal release tape and transferred by thermo-compression printing [35] onto highly doped Si covered with 380 nm SiO_2 film. Multilayer flakes with thickness ranging from 30 to 50 nm (basing on AFM analyses) have been used in these experiments.

Soft O_2 plasma treatments of MoS_2 surface were carried out with a commercial ICP system (Roth & Rau Microsys 400). The plasma was generated with 100 W power and an Ar(20%)/O_2(80%) gas mixture. The Ar percentage in this gas mixture is the lowest allowing to generate a stable plasma with our equipment. The plasma source is located at approx. 20 cm above the sample and no bias is applied to the sample during the process. Under these conditions, physical etching effects by energetic ions are avoided, and

only a chemical action by the plasma is obtained. The base pressure in the chamber before starting the process was 2×10^{-6} mbar, whereas the pressure during the plasma process was 3×10^{-3} mbar.
Test device structures for CAFM analyses consisted of metal films with circular holes open on MoS_2 flakes to allow scanning with the CAFM tip. These structures were fabricated by photolithography and lift-off of a Ni(20nm)/Au(80 nm) bilayer.
Back-gated FETs on pristine MoS_2 were fabricated by conventional lift-off of Ni(20nm)/Au(80 nm) to obtain the source/drain contacts. FETs with O_2 plasma functionalized source/drain contact areas were fabricated using a self-aligned process consisting of the following steps: (i) spin coating of 1 μm positive photoresist film (AR5350 from Allresist GmbH) onto MoS_2; (ii) photolithography to open the resist in the source/drain contacts areas; (iii) soft O_2 plasma treatment; (iv) deposition of a Ni(20nm)/Au(80 nm) bilayer; (v) lift-off of the resist in acetone. Hence, the only difference with respect to the conventional lift-off process is the introduction of the soft O_2 plasma treatment. It is worth noting that such soft plasma process, does not degrade significantly the 1 μm thick resist film. This allows using it both as a "hard-mask" for plasma and for the subsequent lift-off process, after contacts deposition.

AFM and CAFM measurements. AFM and CAFM measurements were carried out with a DI3100 System with Nanoscope V controller. Pt coated ultra-sharp tips (curvature radius ~10 nm) were used for CAFM analyses.

XPS. X-ray Photoelectron Spectroscopy (XPS) spectra were recorded with a PHI 5000 VersaProbe II scanning XPS Microprobe™ (ULVAC-PHI, Inc.) using monochromatic Al-Kα radiation (hν = 1486.6 eV) from an X-ray source operating at 100 μm spot size, 25 W power and 15 kV acceleration voltage. A surface XPS survey was collected with the hemispherical analyzer (128 channels) at the pass energy of 23.500 eV, energy step size of 0.050 eV; the photoelectron take off angles with respect to the surface were 45°; Data analysis was performed with Multipak software version 9.7 (ULVAC-PHI). Binding energy values are obtained using adventitious hydrocarbon as reference (248.8 eV).

Atomic resolution STEM and EELS. STEM and atomic EELS measurements were performed using a sub-Angstrom aberration-corrected JEOL ARM200F microscope, which consists of a probe corrected STEM microscope equipped with a C-FEG and a fully loaded GIF Quantum ER as EELS spectrometer. A 60-keV primary beam energy with a probe size of 0.12 nm was used for the analyses. EELS spectra

were recorded in dual-EELS mode, i.e, by simultaneous acquisition of core-loss and low-loss spectra for precise energy scale calibration, and with a dispersion of 0.325 eV/pixel.

Transistors characterization. Electrical characterization of the back-gated FETs was carried out at room temperature (300 K) in dark conditions and under nitrogen flux using a Cascade Microtech probe station with an Agilent 4156b parameter analyzer.

DFT calculations. Band structure calculations were performed within the density functional theory using the SIESTA code [36]. We used the Perdew-Burke-Ernzerhof implementation [37] of the generalized gradient approximation for the description of the electronic correlations along with standard norm-conserving pseudopotentials [38] and a double-ζ plus polarization basis set for all elements. For the modeling of oxygen inclusions and defects (substitutional and interstitial) within a MoS_2 crystal we considered (3×3) bilayer and trilayer 2H-MoS_2 supercells with a variable concentration of O atoms (see figure 5 of the main text and S3 of the supplementary information). A (4×4×1) Monkhorst-Pack grid was used for the Brillouin zone sampling. For the modeling of the MoO_3/MoS_2 system and in order to obtain a quasi-commensurate interface, we considered a junction between a (2×4) rectangular monolayer MoS_2 supercell and a (3×3) monolayer MoO_3 supercell (see figure S5). In this way the remaining uniaxial stress components of the MoO_3 crystal were 1.6% along the x-axis and -3.9% along the y-axis with respect to the unstrained values. A (2×2×1) Monkhorst-Pack grid was used here for the Brillouin zone sampling. In all cases, real space integrals were evaluated on a mesh with a cut-off energy of 210 Ry, while atomic relaxation was imposed until forces were less than 0.04 eV/Å. By completion of the self-consistent calculations, the band structures were unfolded to the respective first Brillouin zones following the methodology of ref. [39]. Simulations of the core-loss EELS spectra of bulk MoS_2 were performed with the all-electron WIEN2K code [40], considering the same exchange-correlation functional as before. Electronic convergence was achieved using a plane-wave cut-off parameter $R_{MT}K_{max}$=7 and a sampling of the Brillouin zone with 384 irreducible k-points. The EELS spectra were computed with the TELNES3 post-processing program using a Gaussian broadening of 0.5 eV.

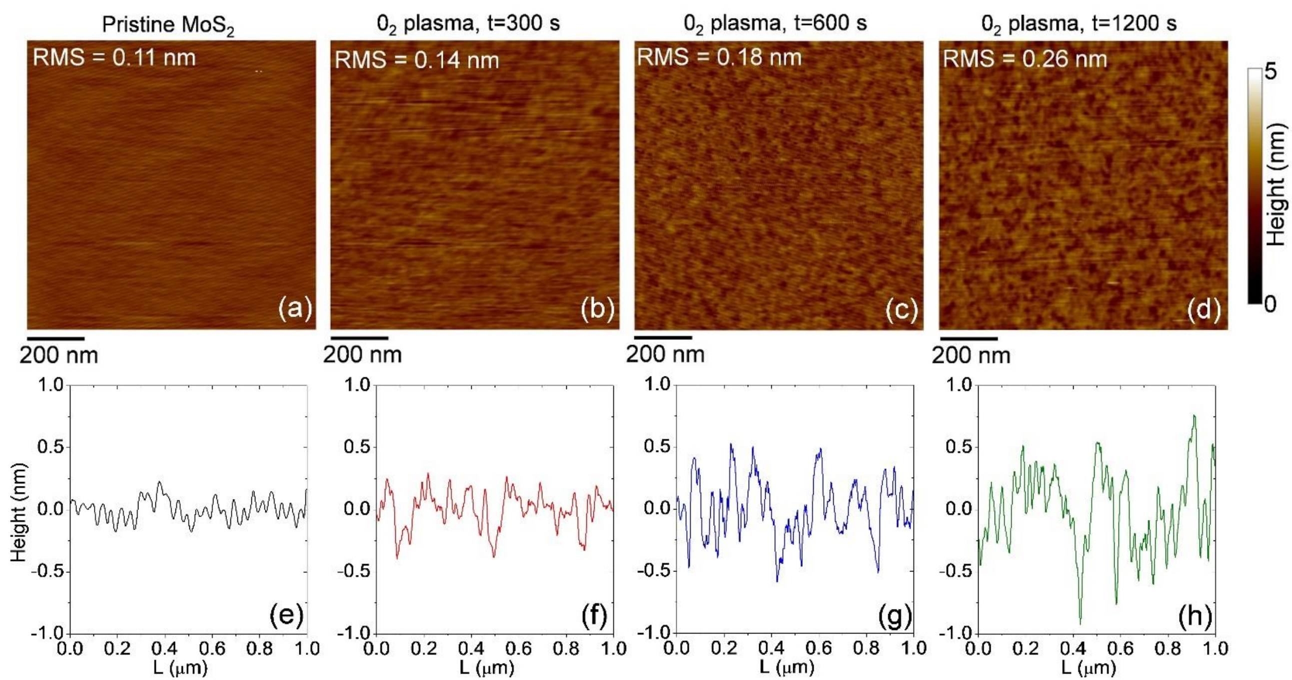

Figure 1

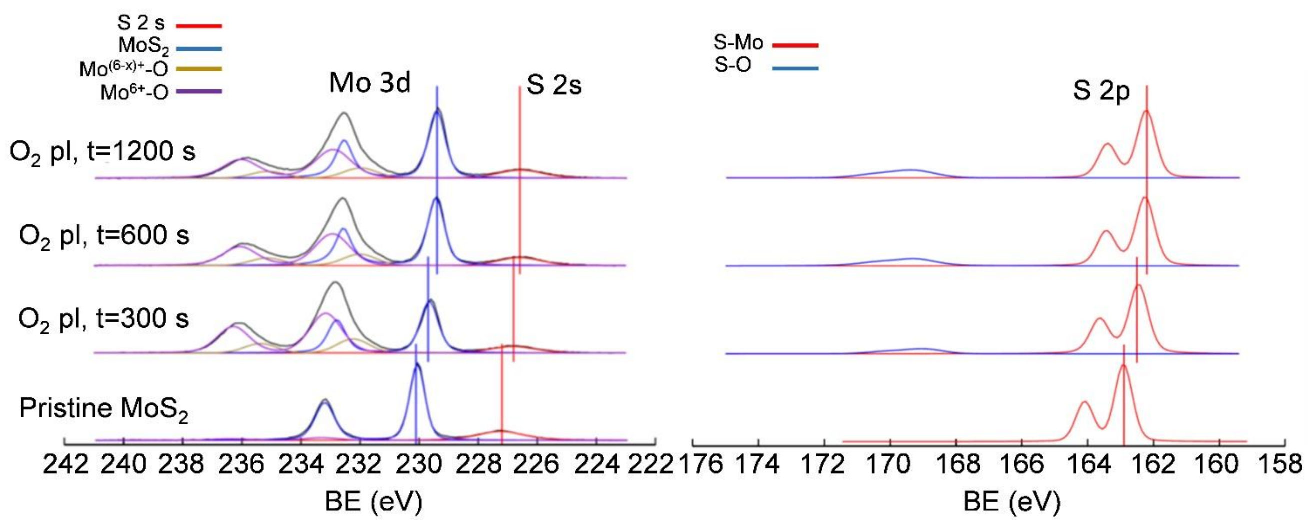

Figure 2

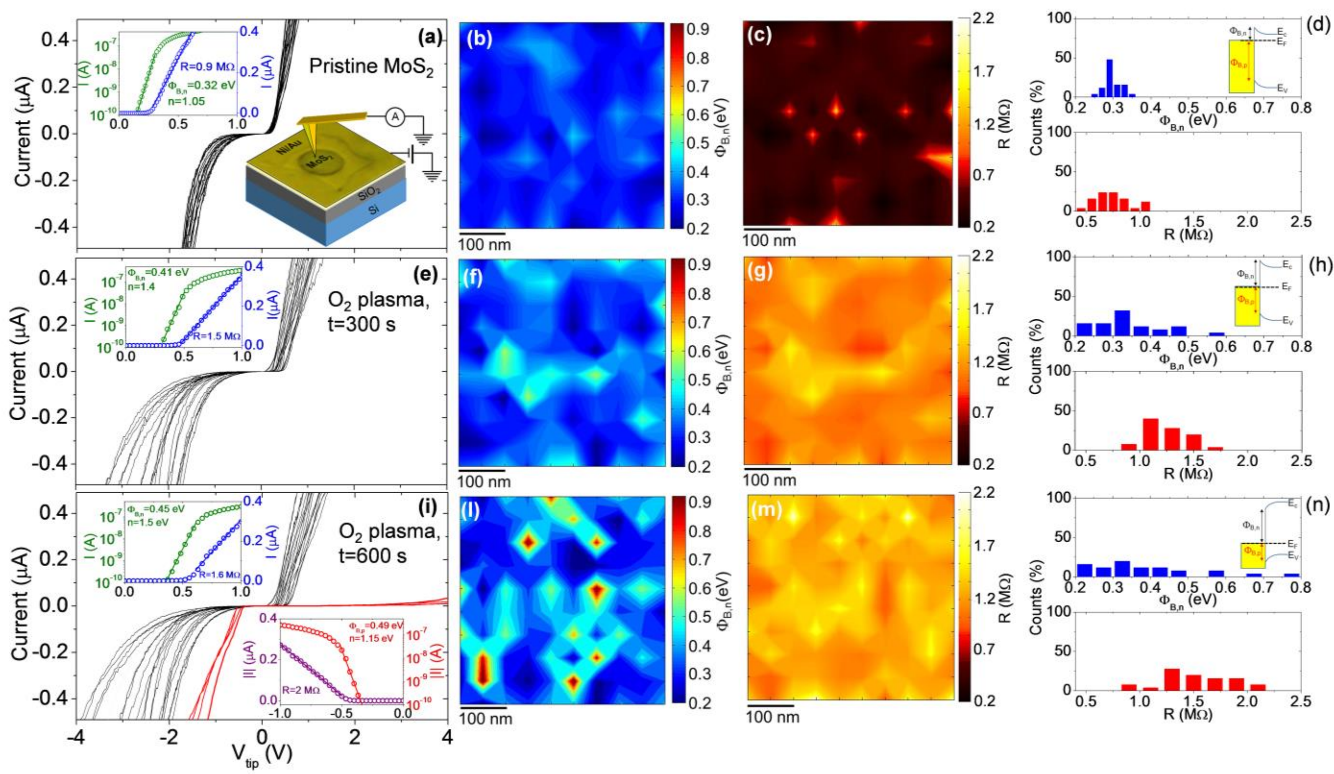

Figure 3

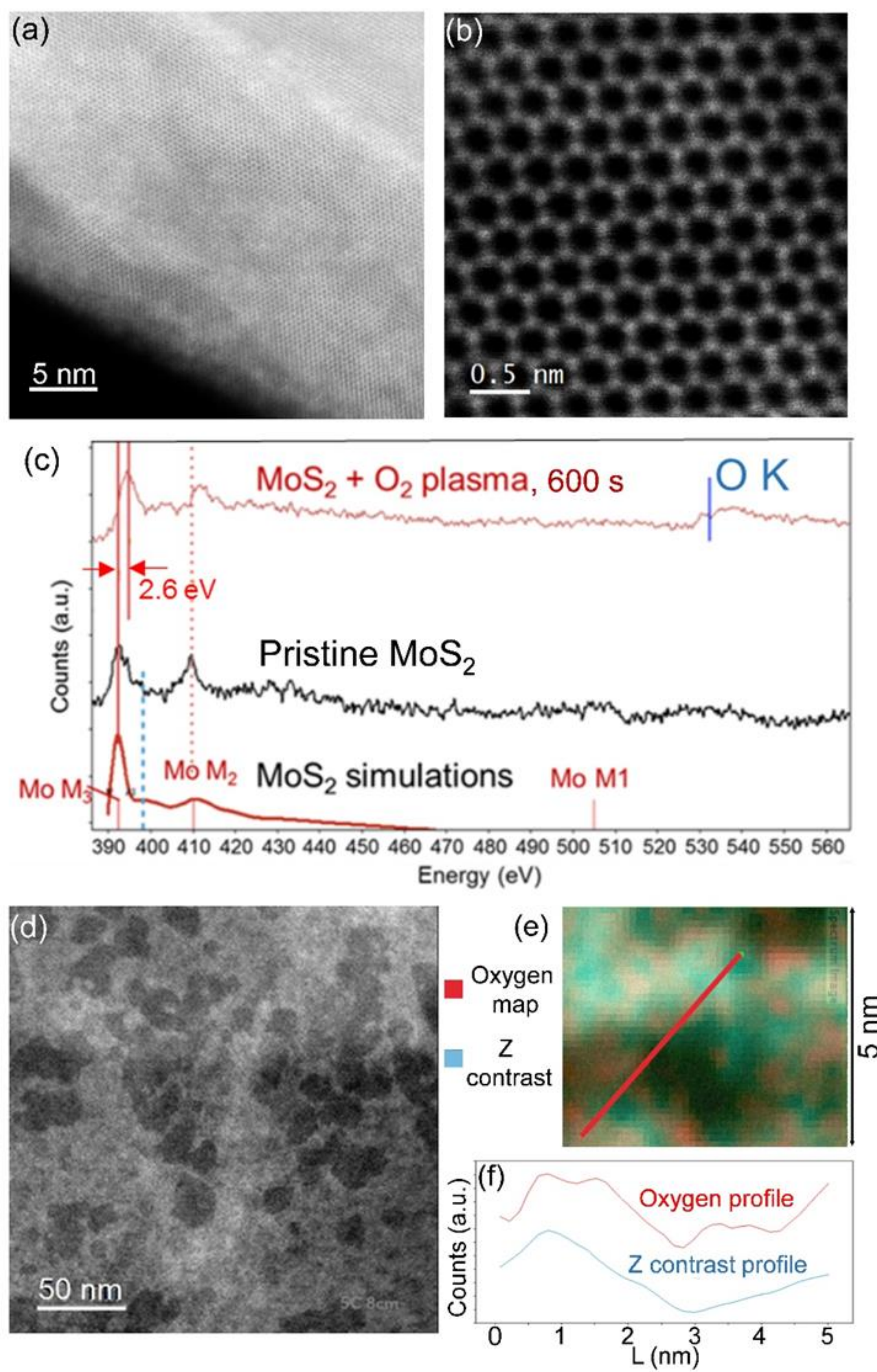

Figure 4

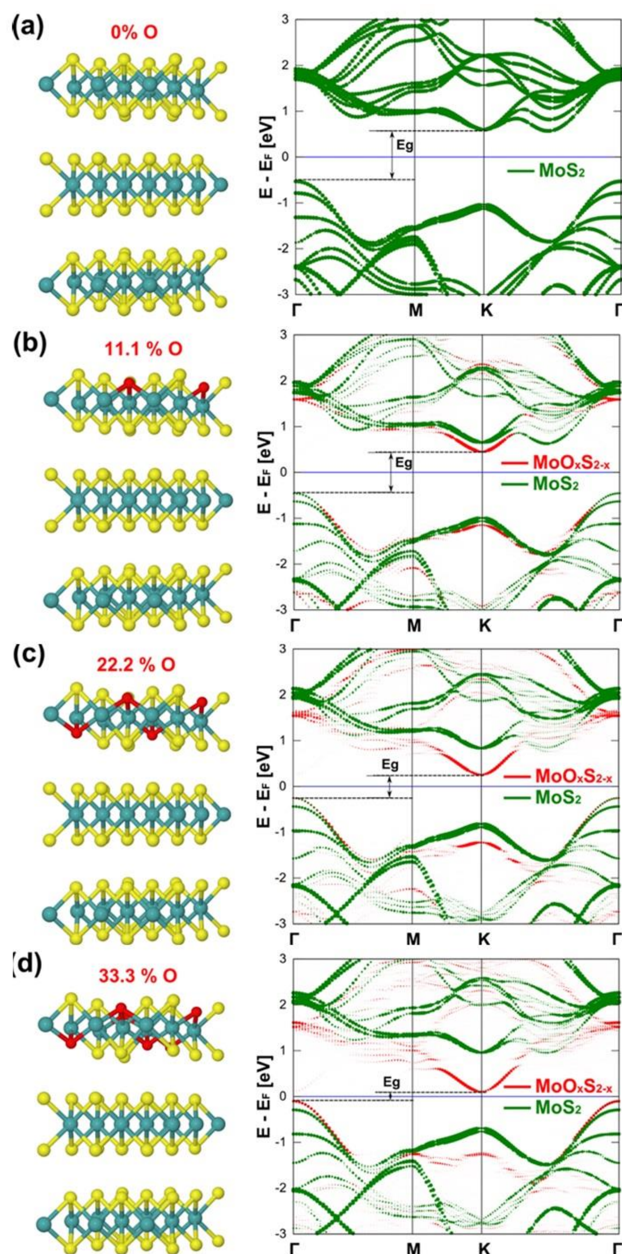

(a)
0% O
E - E$_F$ [eV]
Eg
MoS$_2$
Γ
M
K
(b)
11.1 % O
MoO$_x$S$_{2-x}$
(c)
22.2 % O
(d)
33.3 % O

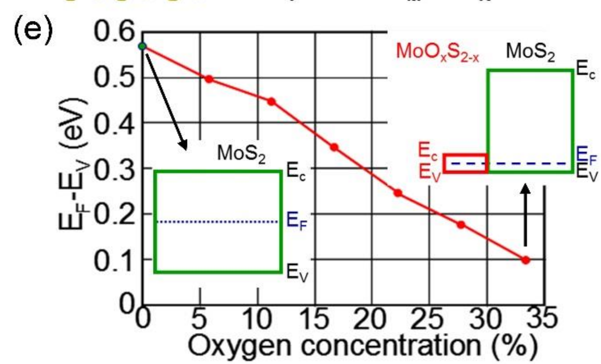

(e)
E_F-E_V (eV)
Oxygen concentration (%)
MoS$_2$
E_c
E_F
E_V
MoO$_x$S$_{2-x}$

Figure 5

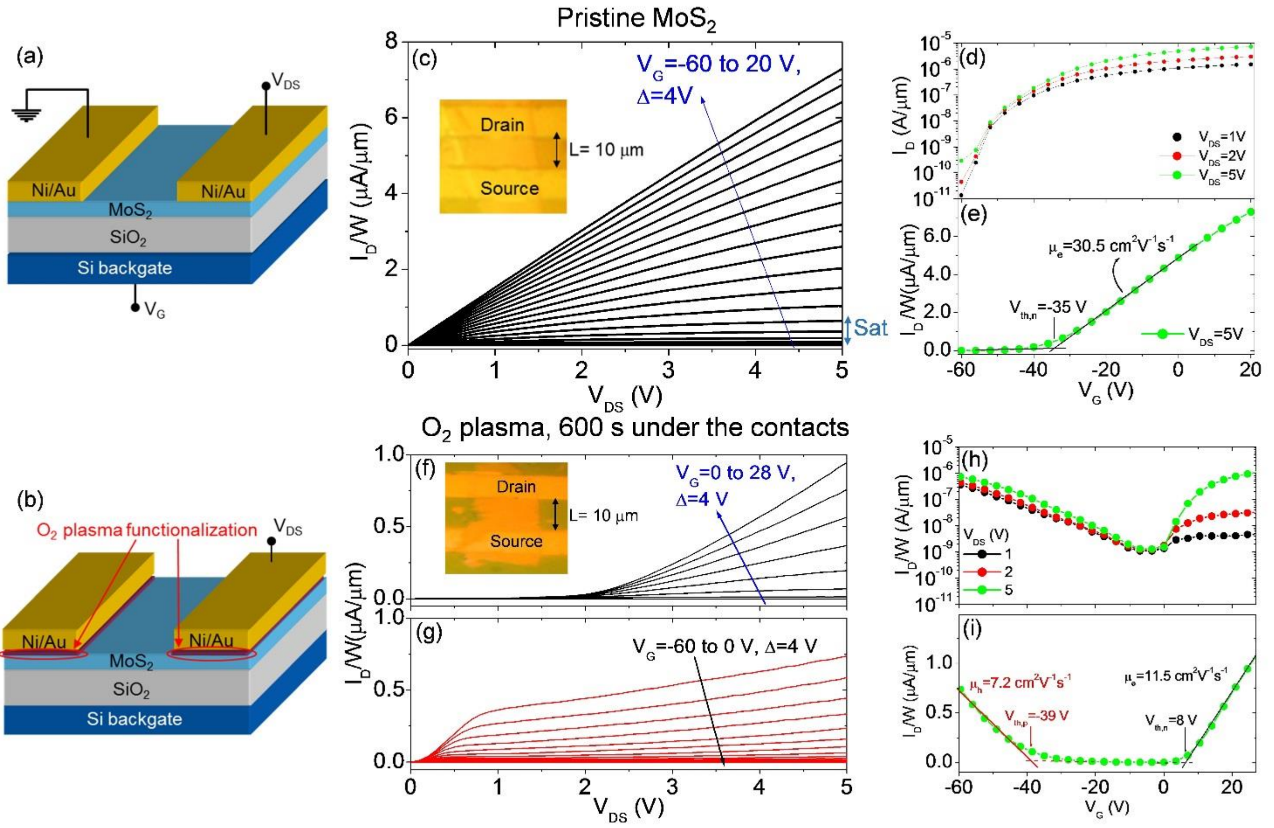

Figure 6

Figure Captions:

Fig.1 AFM morphology of as-exfoliated MoS_2 (a) and of MoS_2 samples subjected to O_2 plasma for 300 s (b), 600 s (c) and 1200 s (d). The root mean square (RMS) roughness values calculated from the four topography maps are also reported. Representative height line-scans are reported in (e)-(h).

Fig.2 XPS spectra of Mo *3d*, S *2s* (left panel) and S *2p* core levels (right panel) collected on as-exfoliated MoS_2 samples and after O_2 plasma treatments for 300 s, 600 s and 1200 s.

Fig.3 Arrays of local current-voltage ($I-V_{tip}$) characteristics measured by CAFM on pristine MoS_2 (a) and on the samples subjected to O_2 plasma for 300 s (e) and 600 s (i). The setup for local I-V measurements is illustrated in the lower left insert of panel (a). The upper-right insert of panel (a) shows the fit of a representative $I-V_{tip}$ curve for pristine MoS_2, both on linear and semilog-scale, to extract the local Schottky barrier height ($\Phi_{B,n}$), ideality factor (n) and the series resistance (R). Similar fitting has been carried out also for the samples subjected 300 s and 600 s O_2 plasma (inserts of panel (e) and (i)). Two dimensional (2D) maps of the local $\Phi_{B,n}$ (b) and R (c) values and hystograms of $\Phi_{B,n}$ and R (d) on pristine MoS_2. 2D maps of the local $\Phi_{B,n}$ (f) and R (g) values and hystograms of $\Phi_{B,n}$ and R (h) after 300 s O_2 plasma. 2D maps of the local $\Phi_{B,n}$ (l) and R (m) values and hystograms of $\Phi_{B,n}$ and R (n) after 600 s O_2 plasma.

Fig.4 Atomic resolution STEM analyses at different magnifications (a) and (b) performed close to the edge of few layers MoS_2 flakes subjected to this O_2 plasma functionalization for 600s. (c) Representative EELS spectra collected on pristine MoS_2 samples and on MoS_2 flakes subjected to 600 s O_2 plasma treatment. Signal background subtraction and plural-scattering deconvolution have been performed by applying the power-law background fitting and Fourier-ratio method respectively. A calculated EELS spectrum for MoS_2 is included. (d) Z-contrast image collected at low magnification on a multilayer MoS_2 flake, where the dark grey patches are sub-monolayer etched areas on MoS_2 surface produced by the soft O_2 plasma. (e) Representative spectrum image at the border of a patch: the oxygen map (obtained by integration of the O K edge signal) is overlapped to the Z-contrast map. (f) Intensity linescans of oxygen concentration and Z contrast extracted from the spectrum image in (e)

Fig.5 Structural configuration and electronic structure calculations for a trilayer of MoS_2 with four different atomic percentage of substitutional oxygen included in the topmost layer: 0%, *i.e.* pristine MoS_2

(a), 11.1% (b), 22.2% (c), 33.3% (d). Dependence of E_F-E_V on the oxygen percentage in the topmost MoO_xS_{2-x} layer (e).

Fig.6 Schematic illustrations of back-gated field effect transistors (FETs) with source and drain contacts deposited on pristine MoS_2 (a) or on areas selectively exposed to O_2 plasma for an optimal time of 600 s (b). (c) I_D-V_{DS} characteristics (for V_G from -60 to 20 V) measured on a FET with channel length L=10 μm fabricated with a pristine multilayer MoS_2 flake (~40 nm thick). An optical microscopy of the device is shown in the insert. Semilog-scale (d) and linear scale (e) plots of the I_D-V_G characteristics for the pristine MoS_2 FET. The threshold voltage and the field effect mobility were extracted by fitting of the linear scale I_D-V_G. I_D-V_{DS} characteristics for V_G from 0 to 28 V (f) and for V_G from -60 to 0 V (g) measured on a FET with channel length L=10 μm fabricated with a multilayer MoS_2 flake (~40 nm thick) subjected to O_2 plasma functionalization for 600 s. An optical microscopy of the device is also shown in the insert. Semilog-scale (h) and linear scale (i) plots of the I_D-V_G characteristics for the FET with O2 functionalized contact areas. The threshold voltages for n-type and p-type current transport and the field effect mobilities for electrons and holes were extracted by fitting the electrons and current branches of the ambipolar I_D-V_G characteristic on linear scale.

References

[1] Radisavljevic, B.; Radenovic, A.; Brivio, J.; Giacometti, V.; Kis, A. Single-Layer MoS_2 Transistors. *Nat. Nanotechnol.* **2011**, *6*, 147-150.

[2] Kim, S.; Konar, A.; Hwang, W. S.; Lee, J. H.; Lee, J.; Yang, J.; Jung, C.; Kim, H.; Yoo, J. B.; Choi, J. Y.; Jin, Y. W.; Lee, S. Y.; Jena, D.; Choi, W.; Kim, K. High-Mobility and Low-Power Thin-Film Transistors Based on Multilayer MoS_2 Crystals. *Nat. Commun.* **2012**, *3*, 1011.

[3] Desai, S. B.; Madhvapathy, S. R.; Sachid, A. B.; Llinas, J. P.; Wang, Q.; Ahn, G. H.; Pitner, G.; Kim, M. J.; Bokor, J.; Hu, C.; Wong, H.-S. P.; Javey, A. MoS_2 Transistors with 1-Nanometer Gate Lengths. *Science* **2016**, 354, 99-102.

[4] Nourbakhsh, A.; Zubair, A.; Sajjad, R. N.; Tavakkoli, K. G. A.; Chen, W.; Fang, S.; Ling, X.; Kong, J.; Dresselhaus, M. S.; Kaxiras, E.; Berggren, K. K.; Antoniadis, D.; Palacios, T. MoS_2 Field-Effect Transistor with Sub-10 nm Channel Length. *Nano Lett.* **2016**, 16, 7798−7806.

[5] K. Alam, Roger K. Lake, Monolayer MoS_2 Transistors Beyond the Technology Road Map, *IEEE Trans. Electron Devices* **2012**, 59, 3250-3254.

[6] Das, S.; Chen, H.-Y.; Penumatcha, A. V.; Appenzeller, J. High Performance Multi-layer MoS_2 Transistors with Scandium Contacts. *Nano Lett.* **2013**, *13*, 100–105.

[7] McDonnell, S.; Addou, R.; Buie, C.; Wallace, R. M.; Hinkle, C. L. Defect-Dominated Doping and Contact Resistance in MoS_2. *ACS Nano* **2014**, *8*, 2880-2888.

[8] Giannazzo, F.; Fisichella, G.; Piazza, A.; Agnello, S.; Roccaforte, F. Nanoscale Inhomogeneity of the Schottky Barrier and Resistivity in MoS_2 Multilayers. *Phys. Rev. B* **2015**, *92*, 081307(R).

[9] Kappera, R.; Voiry, D.; Yalcin, S. E.; Branch, B.; Gupta, G.; Mohite, A. D.; Chhowalla, M. Phase-Engineered Low-Resistance Contacts for Ultrathin MoS_2 Transistors. *Nat. Mater.* **2014**, 13, 1128-1134.

[10] Kappera, R.; Voiry, D.; Yalcin, S. E.; Jen, W.; Acerce, M.; Torrel, S.; Branch, B.; Lei, S.; Chen, W.; Najmaei, S.; Lou, J.; Ajayan, P. M.; Gupta, G.; Mohite, A. D.; Chhowalla, M. Metallic 1T Phase Source/Drain Electrodes for Field Effect Transistors from Chemical Vapor Deposited MoS_2. *APL Mater.* **2014**, 2, 092516.

[11] Das, S.; Prakash, A.; Salazar, R.; Appenzeller, J. Toward Low-Power Electronics: Tunneling Phenomena in Transition Metal Dichalcogenides. *ACS Nano* **2014**, *8*, 1681-1689.

[12] Giannazzo, F.; Fisichella, G.; Piazza, A.; Di Franco, S.; Greco, G.; Agnello, S.; Roccaforte, F. Effect of Temperature–Bias Annealing on the Hysteresis and Subthreshold Behavior of Multilayer MoS_2 Transistors. *Phys. Status Solidi RRL* **2016**, *10*, 797–801.

[13] Chuang, S.; Battaglia, C.; Azcatl, A.; McDonnell, S.; Kang, J. S.; Yin, X.; Tosun, M.; Kapadia, R.; Fang, H.; Wallace, R. M.; Javey, A. MoS_2 P‑Type Transistors and Diodes Enabled by High Work Function MoO_x Contacts, *Nano Lett.* **2014**, *14*, 1337−1342.

[14] McDonnell, S.; Azcatl, A.; Addou, R.; Gong, C.; Battaglia, C.; Chuang, S.; Cho, K.; Javey, A.; Wallace, R. M. Hole Contacts on Transition Metal Dichalcogenides: Interface Chemistry and Band Alignments. *ACS Nano* **2014**, *8*, 6265–6272.

[15] Dolui, K.; Rungger, I.; Pemmaraju, C. D.; Sanvito, S. Possible Doping Strategies for MoS_2 Monolayers: An Ab Initio study. *Phys. Rev. B* **2013**, 88, 075420.

[16] Suh, J.; Park, T.-E.; Lin, D.-Y.; Fu, D.; Park, J.; Jung, H. J.; Chen, Y.; Ko, C.; Jang, C.; Sun, Y.; Sinclair, R.; Chang, J.; Tongay, S.; Wu, J. Doping against the Native Propensity of MoS_2: Degenerate Hole Doping by Cation Substitution. *Nano Lett.* **2014**, *14*, 6976-6982.

[17] Das, S.; Demarteau, M.; Roelofs, A. Nb-Doped Single Crystalline MoS_2 Field Effect Transistor. *Appl. Phys. Lett.* **2015**, *106*, 173506.

[18] Nipane, A.; Karmakar, D.; Kaushik, N.; Karande, S.; Lodha, S. Few-Layer MoS_2 p-type Devices Enabled by Selective Doping Using Low Energy Phosphorus Implantation, *ACS Nano* **2016**, 10, 2128−2137.

[19] Liu, X.; Qu, D.; Ryu, J.; Ahmed, F.; Yang, Z.; Lee, D.; Yoo, W. J. P-Type Polar Transition of Chemically Doped Multilayer MoS_2 Transistor. *Adv. Mater.* **2016**, *28*, 2345–2351.

[20] Islam, M. R.; Kang, N.; Bhanu, U.; Paudel, H. P.; Erementchouk, M.; Tetard, L.; Leuenberger, M. N.; Khondaker, S. I. Tuning the Electrical Property via Defect Engineering of Single Layer MoS_2 by Oxygen Plasma. *Nanoscale* **2014**, *6*, 10033-10039.

[21] Khondaker, S. I.; Islam, M. R. Bandgap Engineering of MoS_2 Flakes via Oxygen Plasma: A Layer Dependent Study. *J. Phys. Chem.* C **2016**, *120*, 13801−13806.

[22] Nan, H.; Wang, Z.; Wang, W.; Liang, Z.; Lu, Y.; Chen, Q.; He, D.; Tan, P.; Miao, F.; Wang, X.; Wang, J.; Ni, Z. Strong Photoluminescence Enhancement of MoS_2 through Defect Engineering and Oxygen Bonding. *ACS Nano* **2014**, *8*, 5738–5745.

[23] Kang, N.; Paudel, H. P.; Leuenberger, M. N.; Tetard, L.; Khondaker, S. I. Photoluminescence Quenching in Single-Layer MoS_2 via Oxygen Plasma Treatment. *J. Phys. Chem. C* **2014**, 118, 21258−21263.

[24] Chen, M.; Nam, H.; Wi, S.; Ji, L.; Ren, X.; Bian, L.; Lu, S.; Liang, X. Stable Few-Layer MoS_2 Rectifying Diodes Formed by Plasma-Assisted Doping. *Appl. Phys. Lett.* **2013**, *103*, 142110.

[25] Wi, S.; Kim, H.; Chen, M.; Nam, H.; Guo, L. J.; Meyhofer, E.; Liang, X. Enhancement of Photovoltaic Response in Multilayer MoS_2 Induced by Plasma Doping. *ACS Nano* **2014**, *8*, 5270–5281.

[26] Zhu, H.; Qin, X.; Cheng, L.; Azcatl, A.; Kim, J.; Wallace, R. M. Remote Plasma Oxidation and Atomic Layer Etching of MoS_2. *ACS Appl. Mater. Interfaces* **2016**, *8*, 19119−19126.

[27] Werfel, W.; Minni, E. Photoemission Study of the Electronic Structure of Mo and Mo Oxides. *J. Phys. C: Solid State Phys.* **1983**, *16*, 6091-6100.

[28] Greiner, M. T.; Chai, L.; Helander, M. G.; Tang, W.-M.; Lu, Z.- H. Metal/Metal-Oxide Interfaces: How Metal Contacts Affect the Work Function and Band Structure of MoO_3. *Adv. Funct. Mater.* **2013**, *23*, 215-226.

[29] Song, Z.; Cai, T.; Chang, Z.; Liu, G.; Rodriguez, J. A.; Hrbek, J. Molecular Level Study of the Formation and the Spread of MoO_3 on Au(111) by Scanning Tunneling Microscopy and X-Ray Photoelectron Spectroscopy. *J. Am. Chem. Soc.* **2003**, *125*, 8059-8066.

[30] Fleisch, T. H.; Mains, G. J. An XPS Study of the UV Reduction and Photochromism of MoO_3 and WO_3. *J. Chem. Phys.* **1982**, *76*, 780-786.

[31] Yamamoto, M.; Einstein, T. L.; Fuhrer, M. S.; Cullen, W. G. Anisotropic Etching of Atomically Thin MoS_2, *J. Phys. Chem. C* **2013**, 117, 25643–25649.

[32] Piazza, A., Giannazzo, F.; Buscarino, G.; Fisichella, G.; La Magna, A.; Roccaforte, F.; Cannas, M.; Gelardi, F. M.; Agnello, S. In-Situ Monitoring by Raman Spectroscopy of the Thermal Doping of Graphene and MoS_2 in O_2-Controlled Atmosphere. *Beilstein J. Nanotechnol.* **2017,** *8,* 418–424.

[33] Lajaunie, L.; Boucher, F.; Dessapt, R.; Moreau, P. Quantitative Use of Electron Energy-Loss Spectroscopy Mo-$M_{2,3}$ Edges for the Study of Molybdenum Oxides. *Ultramicroscopy* **2015**, *149*, 1-8.

[34] Giannazzo, F.; Fisichella, G.; Piazza, A.; Di Franco, S.; Greco, G.; Agnello, S.; Roccaforte, F. Impact of Contact Resistance on the Electrical Properties of MoS_2 Transistors at Practical Operating Temperatures. *Beilstein J. Nanotechnol.* 2017, 8, 254–263.

[35] Giannazzo, F; Fisichella, G.; Piazza, A.; Di Franco, S.; Oliveri, I. P.; Agnello, S.; Roccaforte, F. Current Injection from Metal to MoS_2 Probed at Nanoscale by Conductive Atomic Force Microscopy. *Mater. Sci. Semicond. Process.* **2016**, *42*, 174–178.

[36] Soler, J. M.; Artacho, E.; Gale, J. D.; García, A.; Junquera, J.; Ordejón, P.; Sánchez-Portal, D. The SIESTA Method for Ab Initio Order-N Materials Simulation. *J. Phys.: Condens. Matter* **2002**, *14*(11), 2745-2779.

[37] Perdew, J. P.; Burke, K.; Ernzerhof, M. Generalized Gradient Approximation Made Simple. *Phys. Rev. Lett.* **1996**, *77*(18), 3865-3868.

[38] Troullier, N.; Martins, J. L. Efficient Pseudopotentials for Plane-Wave Calculations. *Phys. Rev. B* **1991**, *43*(3), 1993.

[39] Deretzis, I.; Calogero, G.; Angilella, G. G. N.; La Magna, A. Role of Basis Sets on the Unfolding of Supercell Band Structures: From Tight-Binding to Density Functional Theory. *Europhys. Lett.* **2014**, *107*, 27006.

[40] Blaha, P.; Schwarz, K.; Madsen, G. K. H.; Kvasnicka, D.; Luitz, J. WIEN2k: an Augmented Plane Wave + Local Orbitals Program for Calculating Crystal Properties. *Vienna: Technische Universität Wien 2001.*